

Probing new physics scenarios using high energy events at NOvA far detector

Chinmay Bera^{1,*} and K. N. Deepthi^{1,†}

¹*Department of Physics, École Centrale School of Engineering
- Mahindra University, Hyderabad, Telangana, 500043, India*

Abstract

NuMI Off-axis ν_e Appearance (NOvA) experiment is an ongoing long baseline neutrino oscillation experiment. The primary channels of interest are the ν_e , $\bar{\nu}_e$ appearance, ν_μ , $\bar{\nu}_\mu$ disappearance channels analyzed in the energy window $1 < E_\nu < 4$ GeV. However, NOvA far detector sees non-trivial high energy ν_e , $\bar{\nu}_e$ events in the energy range $4 < E_\nu < 20$ GeV. These high energy events provide us with an opportunity to investigate the subleading new physics scenarios. In this context, we study the sensitivity of the NOvA experiment to constrain the non-standard interaction (NSI) parameters and environmental decoherence. We observe that by including high energy events (signal + background) the degeneracy around $\epsilon_{e\tau} \sim 1.6$ can be removed throughout the δ_{CP} and $\delta_{e\tau}$ range. Further, we examine the role of signal versus beam background events in removing this degeneracy. In addition, we constrain the decoherence parameter Γ considering events from $1 < E_\nu < 20$ GeV. Later, assuming the presence of decoherence in nature we obtain the allowed regions in θ_{23} and δ_{CP} plane.

* Email Address: chinmay20pphy014@mahindrauniversity.edu.in

† Email Address: nagadeepthi.kuchibhatla@mahindrauniversity.edu.in

I. Introduction

The discovery of the neutrino oscillation phenomenon has established that neutrinos do have a (tiny) mass. This overwhelming evidence challenges the boundaries of the standard model (SM) of particle physics and motivates us to search for a more consistent theory. In this context, the study of new physics scenarios (contributions from sub-leading effects) are crucial as they provide the explanation to beyond the standard model (BSM) physics phenomenon. The ongoing and upcoming high precision neutrino oscillation experiments play pivotal role in the quest for new physics phenomenon. In this work, we analyze the far detector (FD) simulated events at NOvA experiment in the presence of two new physics (NP) paradigms, non-standard interactions (NSIs) [1–3] and environmental decoherence [4–6]. Here we consider individual effect of NSI and environmental decoherence on the neutrino propagation.

Environmental decoherence is the phenomenon that arises due to the interaction of neutrinos with the stochastic environment during propagation. This interaction leads to the loss of coherence among the neutrino mass states¹. Additionally, neutrinos could interact with earth matter via non-standard interactions (NSI) (cannot be explained in the SM scenarios). Both the phenomenon, NSI and environmental decoherence, play a sub-leading (but significant) role in the standard neutrino oscillation framework.

Several studies have discussed neutrino oscillations in the framework of NSI and decoherence. Here, we provide some references relevant to the NOvA experiment. In ref. [7] authors have pointed out the tension in latest NOvA and T2K results [8, 9] could be improved considering NSI in the analysis². Recent analysis of NOvA data [8] ($1 < E_\nu < 5$ GeV) in the presence of NSI have reported NSI parameters $\epsilon_{e\mu} \leq 0.3$, $\epsilon_{e\tau} \leq 0.4$ and revealed a degeneracy of coupling parameter $\epsilon_{e\tau} > 1$ [11]. In ref. [12] authors have extended the latest NOvA standard oscillation result, by adding NSI phenomenon and shown that $\epsilon_{e\tau}$ encounters degeneracy for full range of standard CP phase $\delta_{CP} \in [0 : 360^\circ]$ and non-standard CP phase $\delta_{e\tau} \in [0 : 360^\circ]$. On the other hand, authors in ref. [13] have proposed environmental decoherence to explain the shift in θ_{23} from its maximal mixing in the NOvA data. In a recent analysis [14] authors have constrained

¹ This phenomenon is different from the neutrino wave-packet decoherence.

² Considering scalar NSI authors have updated the analysis in the appendix of ref. [10].

decoherence parameters considering $1 < E_\nu < 5$ GeV NOvA FD events. Analyzing high energy appearance events ($1 < E_\nu < 12$ GeV) at NOvA FD, authors in ref. [15] have constrained the standard oscillation parameters and concluded the sensitivity remains almost unaffected. In this paper we analyze events from $1 < E_\nu < 20$ GeV at NOvA FD to study the sensitivity to new physics scenarios namely NSI and environmental decoherence parameters.

In order to analyze the effects of NSI and decoherence at high energy we include the events from high energy tail ($4 < E_\nu < 20$ GeV) along with the events from standard analysis window of NOvA i.e., $1 < E_\nu < 4$ GeV. We employ these events in the determination of NSI parameters $\epsilon_{e\tau}$ and $\epsilon_{e\mu}$ one at a time. Including high energy events we show that the $\epsilon_{e\tau}$ degeneracy observed in ref. [12] can be removed throughout the δ_{CP} and $\delta_{e\tau}$ range. Further, we examine the role of signal versus beam background events in removing this degeneracy. Furthermore, we display the sensitivity to the decoherence parameter (Γ) considering energy power-law dependency ($\Gamma \propto E^n$, where n is the power-law index) and obtain the upper bounds on Γ . We compare the upper bounds obtained from $1 < E_\nu < 4$ GeV with bounds from high energy events ($1 < E_\nu < 20$ GeV). In addition, assuming decoherence in nature we illustrate the uncertainty in the determination of θ_{23} considering events from $1 < E_\nu < 4$ GeV and $1 < E_\nu < 20$ GeV.

This paper is organized as follows: in section II we provide simulation details and analysis method. In section III we show results for effects of NSI at high energy and, in section IV effects of environmental decoherence at high energy. We summarize our results in section V.

II. Simulation details

NOvA is an ongoing long baseline neutrino oscillation experiment that uses NuMI beam facility at Fermilab. The experiment consists of two detectors, one near detector (ND) at the Fermilab site and a far detector (FD) located at Ash River, Minnesota. A NuMI beam (ref. [16]) is delivered with an off-axis angle 14.6 mrad to the FD. The FD is ~ 810 km away from the source and receives a narrow beam with the flux peak ~ 1.8 GeV. This corresponds to first oscillation peak in the atmospheric sector. During propagation from source to detector, neutrinos experience the Earth's crust density ~ 2.84 gm/cm³.

We simulate the NOvA experiment using publicly available GLOBES software packages [17, 18].

In the experimental definition file we adopt fiducial target mass 14 kt. The experiment utilizes total exposure of 13.6×10^{20} POT for ν and 12.5×10^{20} POT for $\bar{\nu}$ which correspond to 6 years of running in ν mode and 3 years of running in $\bar{\nu}$ mode with an hourly-averaged beam power 742 kW. We adopt energy resolution function $\sigma_E = \alpha E + \beta \sqrt{E} + \gamma$, where $\alpha = 0.11(0.09)$, $\beta = 0$, $\gamma = 0$ for e -like (μ like) events [19, 20]. We implement these information and reproduce the standard event rates as provided in recent NOvA results [8]. To obtain the event spectrum we use the standard parameters listed in table I.

Additionally, to calculate the numerical oscillation probability in the presence of NSI, we deploy *snu.c* [21, 22] extension with GLOBES. On the other hand, we incorporate a *new probability engine* (based on open quantum system) in GLOBES to implement the effect of environmental decoherence.

A. Analysis

For our analysis purpose we include the events from $\nu_\mu (\bar{\nu}_\mu) \rightarrow \nu_e (\bar{\nu}_e)$ and $\nu_\mu (\bar{\nu}_\mu) \rightarrow \nu_\mu (\bar{\nu}_\mu)$ channels as these are the relevant channels to achieve scientific goals at NOvA experiment. We generate true simulated data and test events assuming different hypotheses (in details while present the results); then, we compare them statistically. We mention the details of true and theoretical hypotheses while discuss the respective results. To perform statistical analysis we incorporate Poisson χ^2 function which is defined as

$$\chi^2 = \min_{\alpha_s, \alpha_b} \sum_{\text{channels}} 2 \sum_i \left[N_i^{\text{test}} - N_i^{\text{true}} + N_i^{\text{true}} \log \left(\frac{N_i^{\text{true}}}{N_i^{\text{test}}} \right) \right] + \alpha_s^2 + \alpha_b^2, \quad (2.1)$$

where, N_i^{test} represents the number of test events and N_i^{true} the true events (signal & background) in i -th bin. α_s and α_b are refer to the signal and background normalization errors. We incorporate systematic uncertainties using *pull method* [23, 24].

III. Constraining NSI parameters with $\nu_e/\bar{\nu}_e$ high energy events

Neutrinos interact through weak force as described by the standard model. However, the interactions of neutrinos beyond the SM at a sub-leading level are not completely ruled out. The effect of these non-standard interactions (NSIs) on neutrino oscillation was first introduced

Parameters	True values	Test ranges
$\sin^2 \theta_{12}$	0.307	Fixed
$\sin^2 \theta_{13}$	0.021	[0.02 : 0.02405]
$\sin^2 \theta_{23}$ NH (IH)	0.57 (0.56)	[0.38 : 0.64]
δ_{CP} NH (IH)	0.82π (1.52π)	[0 : 2π]
$\frac{\Delta m_{21}^2}{10^{-5} \text{ eV}^2}$	7.53	Fixed
$\frac{\Delta m_{32}^2}{10^{-3} \text{ eV}^2}$ NH (IH)	2.41 (-2.45)	$[\pm 2.29 : \pm 2.54]$

TABLE I: True oscillation parameters and 3σ ranges have been considered in our analysis are taken from refs. [8, 25].

by Wolfenstein in ref. [1]. Later on, NSIs have widely been studied in the facet of neutrino physics (see reviews [26–30] and references therein). NSI can modify neutrino production, propagation, and detection, leading to deviations from standard oscillation phenomena. In particular, neutrino propagation is affected by neutral current (NC) NSI³. The new interactions are parameterized in terms of diagonal propagation NSI parameters $\epsilon_{\alpha\alpha}$ and off-diagonal parameters $\epsilon_{\alpha\beta}$ ($= |\epsilon_{\alpha\beta}|e^{i\delta_{\alpha\beta}}$, where $\delta_{\alpha\beta}$ is the non-standard CP phase.).

In this section, considering the impact of NSIs on neutrino propagation, we give an overview of the mathematical formulation of oscillation probability. Taking into account one non-zero off-diagonal NSI parameter among $\epsilon_{e\tau}$ and $\epsilon_{e\mu}$ at a time (neglecting others⁴), we present modified oscillation probabilities and event spectra at the NOvA FD. Further, we analyze the two-dimensional sensitivity by projecting χ^2 in $|\epsilon_{e\tau}|$ (or $|\epsilon_{e\mu}|$) versus standard CP-phase δ_{CP} plane and $|\epsilon_{e\tau}|$ (or $|\epsilon_{e\mu}|$) versus non-standard phase $\delta_{e\tau}$ (or $\delta_{e\mu}$) plane in both the energy window $1 < E_\nu < 4$ GeV and $1 < E_\nu < 20$ GeV.

³ NSI due to charge current (CC) interaction of neutrinos with matter affects the production and detection of neutrinos. In this study, we exclude such impacts, because model independent bounds on the production and detection NSI are typically stronger than the propagation NSI by $\mathcal{O}(1)$.

⁴ Appearance channels are significantly affected by the $\epsilon_{e\tau}$ and $\epsilon_{e\mu}$.

A. Formulation of oscillation probabilities in the presence of NSI

The effective Lagrangian in the case of NC-NSI described by the dimension-six four-fermion operators is in the following form

$$\mathcal{L}_{NC-NSI} = -2\sqrt{2}G_F\epsilon_{\alpha\beta}^{fC}(\bar{\nu}_\alpha\gamma^\mu P_L\nu_\beta)(\bar{f}\gamma_\mu P_C f). \quad (3.1)$$

Here, G_F is the Fermi constant and $\epsilon_{\alpha\beta}^{fC}$ are the NSI parameters, with $\alpha, \beta = e, \mu, \tau$; $f = e, u, d$ and $C = L, R$. The effective Hamiltonian

$$H = \frac{1}{2E} [U \text{diag}(0, \Delta m_{21}^2, \Delta m_{31}^2) U^\dagger + \text{diag}(A, 0, 0) + A\epsilon^m], \quad (3.2)$$

where, Δm_{jk}^2 ($j, k = 1, 2, 3$) are the mass-squared differences, U is the standard PMNS matrix, A is the constant matter potential. ϵ^m represents NSI matrix (3×3) including non-standard matter interaction with elements $\epsilon_{\alpha\beta} \equiv \sum_{f,C} \epsilon_{\alpha\beta}^{fC} \frac{N_f}{N_e}$, where N_f and N_e denote the number density of $f(= e, u, d)$ fermion and electron in the earth matter through which neutrinos propagate. The diagonal elements of ϵ^m are real and off-diagonal elements carry a phase term $\delta_{\alpha\beta}$ in the following form $\epsilon_{\alpha\beta} = |\epsilon_{\alpha\beta}| e^{i\delta_{\alpha\beta}}$.

After diagonalizing, the effective Hamiltonian in eq. (3.2) takes the form

$$\tilde{H} = \frac{1}{2E} \tilde{U} \text{diag}(0, \Delta \tilde{m}_{21}^2, \Delta \tilde{m}_{31}^2) \tilde{U}^\dagger, \quad (3.3)$$

with $\Delta \tilde{m}_{jk}^2$ and \tilde{U} are the effective mass-squared differences and modified PMNS matrix respectively. Considering these effects the modified neutrino oscillation probability can be written as

$$\begin{aligned} P_{\alpha\beta}(L) = & \delta_{\alpha\beta} - 2 \sum_{j>k} \text{Re} \left(\tilde{U}_{\beta j} \tilde{U}_{\alpha j}^* \tilde{U}_{\alpha k} \tilde{U}_{\beta k}^* \right) + 2 \sum_{j>k} \text{Re} \left(\tilde{U}_{\beta j} \tilde{U}_{\alpha j}^* \tilde{U}_{\alpha k} \tilde{U}_{\beta k}^* \right) \cos \left(\frac{\Delta \tilde{m}_{jk}^2}{2E} L \right) \\ & + 2 \sum_{j>k} \text{Im} \left(\tilde{U}_{\beta j} \tilde{U}_{\alpha j}^* \tilde{U}_{\alpha k} \tilde{U}_{\beta k}^* \right) \sin \left(\frac{\Delta \tilde{m}_{jk}^2}{2E} L \right). \end{aligned} \quad (3.4)$$

The expression for \tilde{U} and $\Delta \tilde{m}_{jk}^2$ have been obtained considering non-zero $\epsilon_{e\tau}$ and $\epsilon_{e\mu}$ in the appendix of ref. [31].

B. Oscillation probabilities and event rates in the presence of $\epsilon_{e\tau}$

In this subsection, we extensively discuss the effect of non-zero $\epsilon_{e\tau}$ (assuming all other NSI parameters to be zero) on the ν_e ($\bar{\nu}_e$)-appearance channel and event rates. The approximate ν_μ appearance probability considering series expansion in small parameters $\eta \equiv \frac{\Delta m_{21}^2}{\Delta m_{31}^2}, s_{13}, \epsilon_{e\tau}$ up to the first order as shown below

$$\begin{aligned}
P_{\mu e} = & \frac{2}{\hat{A} - 1} \left[\frac{\eta s_{12} c_{12} s_{13} s_{23} c_{23}}{\hat{A}} \left\{ 1 - \cos\left(\frac{\Delta m_{21}^2 L}{2E}\right) - \cos\left(\frac{\Delta m_{31}^2 L}{2E}\right) + \cos\left(\frac{\Delta m_{32}^2 L}{2E}\right) \right\} + \right. \\
& \eta s_{12} c_{12} s_{23} c_{23}^2 \epsilon_{e\tau} \left\{ -\frac{2 - \hat{A}}{\hat{A}} \cos\left(\frac{\Delta m_{21}^2 L}{2E}\right) - \cos\left(\frac{\Delta m_{31}^2 L}{2E}\right) + \cos\left(\frac{\Delta m_{32}^2 L}{2E}\right) + \frac{2 - \hat{A}}{\hat{A}} \right\} \\
& - s_{13} s_{23}^2 c_{23} \epsilon_{e\tau} \left\{ -\cos\left(\frac{\Delta m_{21}^2 L}{2E}\right) + \frac{\hat{A} + 1}{\hat{A} - 1} \cos\left(\frac{\Delta m_{31}^2 L}{2E}\right) + \cos\left(\frac{\Delta m_{32}^2 L}{2E}\right) - \frac{\hat{A} + 1}{\hat{A} - 1} \right\} \\
& - s_{23}^2 c_{23}^2 \epsilon_{e\tau}^2 \left\{ -\cos\left(\frac{\Delta m_{21}^2 L}{2E}\right) + \frac{\hat{A}}{\hat{A} - 1} \cos\left(\frac{\Delta m_{31}^2 L}{2E}\right) + \hat{A} \cos\left(\frac{\Delta m_{32}^2 L}{2E}\right) - \frac{1}{\hat{A} - 1} - \hat{A} \right\} \\
& \left. - \frac{\hat{A} - 1}{\hat{A}^2} \eta^2 s_{12}^2 c_{12}^2 c_{23}^2 \left\{ \cos\left(\frac{\Delta m_{21}^2 L}{2E}\right) - 1 \right\} - \frac{s_{13}^2 s_{23}^2}{\hat{A} - 1} \left\{ \cos\left(\frac{\Delta m_{31}^2 L}{2E}\right) - 1 \right\} \right] . \quad (3.5)
\end{aligned}$$

Here we use the following abbreviation: $\hat{A} \equiv \frac{A}{\Delta m_{31}^2}$, $s_{ij} \equiv \sin \theta_{ij}$ and $c_{ij} = \cos \theta_{ij}$. We can obtain the probabilities corresponding to $\bar{\nu}_\mu \rightarrow \bar{\nu}_e$ channel replacing $A \rightarrow -A$, $\delta_{CP} \rightarrow -\delta_{CP}$, $\delta_{e\tau} \rightarrow -\delta_{e\tau}$. We present the numerical appearance probability $P_{\mu e}$ ($P_{\bar{\mu} \bar{e}}$) versus neutrino energy E_ν and simulated event rates versus reconstructed energy E_ν^{reco} in fig. 1 using eq. (3.4). Upper and lower rows correspond to $\nu_\mu \rightarrow \nu_e$ and $\bar{\nu}_\mu \rightarrow \bar{\nu}_e$ channels. The plots in the left panel represent probability, while other plots illustrate the event rates. The middle and right panels correspond to events per bin in the energy ranges $1 < E_\nu < 4$ GeV and $4 < E_\nu < 20$ GeV, respectively.

In each of the probability plots (left panel), the black curve represents standard oscillation probability, whereas the blue band refers to oscillation probability embodying the effect of $|\epsilon_{e\tau}| = 0.4$ with the variable non-standard phase $\delta_{e\tau} = [0 : 2\pi]$. The red dotted, magenta dashed and green dot-dashed curves include $|\epsilon_{e\tau}| = 0.4$ with different phases $\delta_{e\tau} = 0, \delta_{e\tau} = \pi/2$ and $\delta_{e\tau} = 3\pi/2$ respectively. For $|\epsilon_{e\tau}| = 0.4$ and $\delta_{e\tau} = 0, 3\pi/2$, $P_{\mu e}$ is higher than the standard oscillation probability as can be seen from red dotted and green dot-dashed lines, respectively. On the other hand, $|\epsilon_{e\tau}| = 0.4, \delta_{e\tau} = \pi/2$ (magenta) shows lower probability w.r.t standard oscillation. In the case of $P_{\bar{\mu} \bar{e}}$ the calculated probability is higher than the standard probability for $\delta_{e\tau} = 0, 3\pi/2$

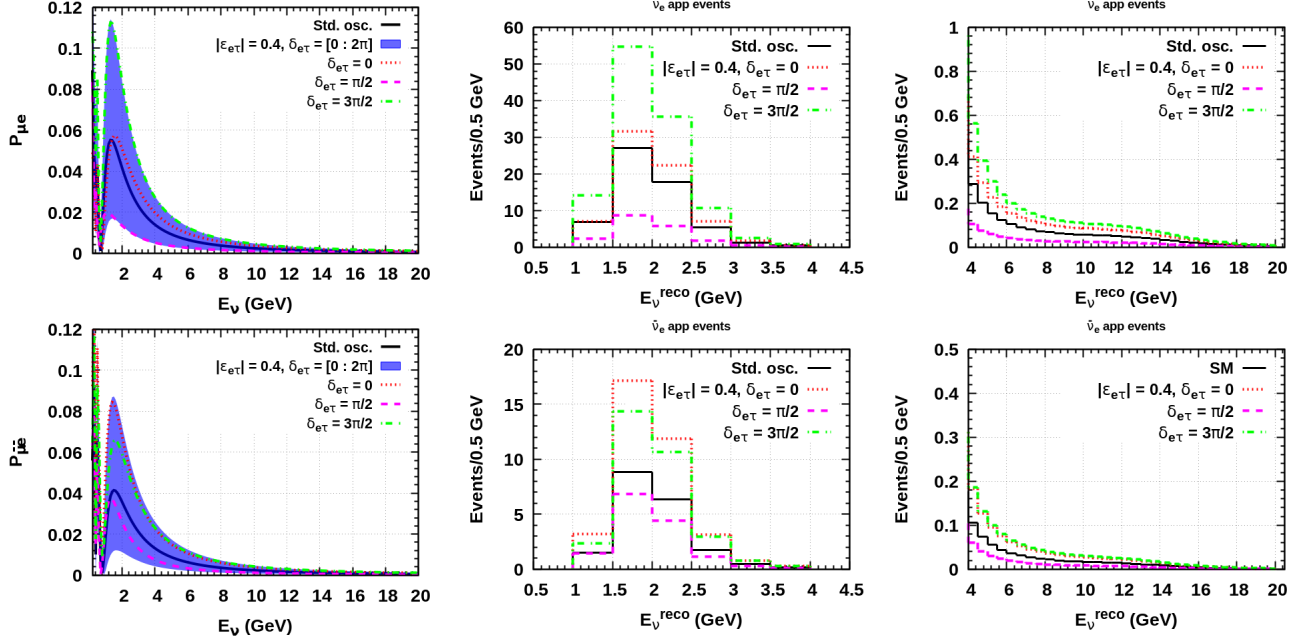


FIG. 1: Appearance probability versus neutrino energy and event rates versus reconstructed energy for ν_e ($\bar{\nu}_e$) in the upper (lower) row. We consider $|\epsilon_{e\tau}| = 0.4$ and corresponding phases to show modified probability and event rates in the presence of non-standard interaction.

and lower than std. osc. for $\delta_{e\tau} = \pi/2$ as can be seen from the red, green and magenta curves respectively. The standard oscillation curve is degenerate with NSI probability for a combination of $|\epsilon_{e\tau}|$ and $\delta_{e\tau}$ throughout the energy range. We notice the overlap between the blue band and solid black curve that indicates degeneracy between NSI ($|\epsilon_{e\tau}|$, $\delta_{e\tau}$) and SM case.

In the middle and right panels we depict events spectra corresponding to ν_e (top row) and $\bar{\nu}_e$ (bottom row) appearance channels. We show event rates related to energy ranges $1 < E_\nu < 4$ GeV (middle) and $4 < E_\nu < 20$ GeV (right). The legends are mentioned in the respective plots.

C. Allowed regions in $\epsilon_{e\tau}$ and $\delta_{CP(e\tau)}$ parameter space

In fig. 2 we show the allowed contours with 95% (1.96 σ) CL in the $|\epsilon_{e\tau}| - \delta_{CP}$ plane (top row) and $|\epsilon_{e\tau}| - \delta_{e\tau}$ plane (bottom row). Plots shown in the left and right panels considering energy analysis energy window $1 < E_\nu < 4$ GeV and $1 < E_\nu < 20$ GeV, respectively. We perform the analysis using standard model scenario in the simulated data and only non-zero $\epsilon_{e\tau}$ in the theory.

We compute $\Delta\chi^2$ as per the definition,

$$\Delta\chi^2 = \chi^2(\epsilon_{e\tau}[true] = 0, \epsilon_{e\tau}[test] \neq 0), \quad (3.6)$$

with true δ_{CP} fixed at 0.82π and marginalize over θ_{13} , θ_{23} , Δm_{31}^2 and $\delta_{e\tau}$. Similarly, we calculate $\Delta\chi^2$ corresponding to $\epsilon_{e\tau}[test]$ versus $\delta_{e\tau}[test]$ contour using eq. 3.6. Here, we marginalize over θ_{13} , θ_{23} , Δm_{31}^2 and δ_{CP} . We vary standard and non-standard CP phase in the full range $0 - 360^\circ$ and show regions with 95% CL for both the normal hierarchy (NH, green regions) and inverted hierarchy (IH, gray region). The unmentioned oscillation parameters are kept fixed to their true values.

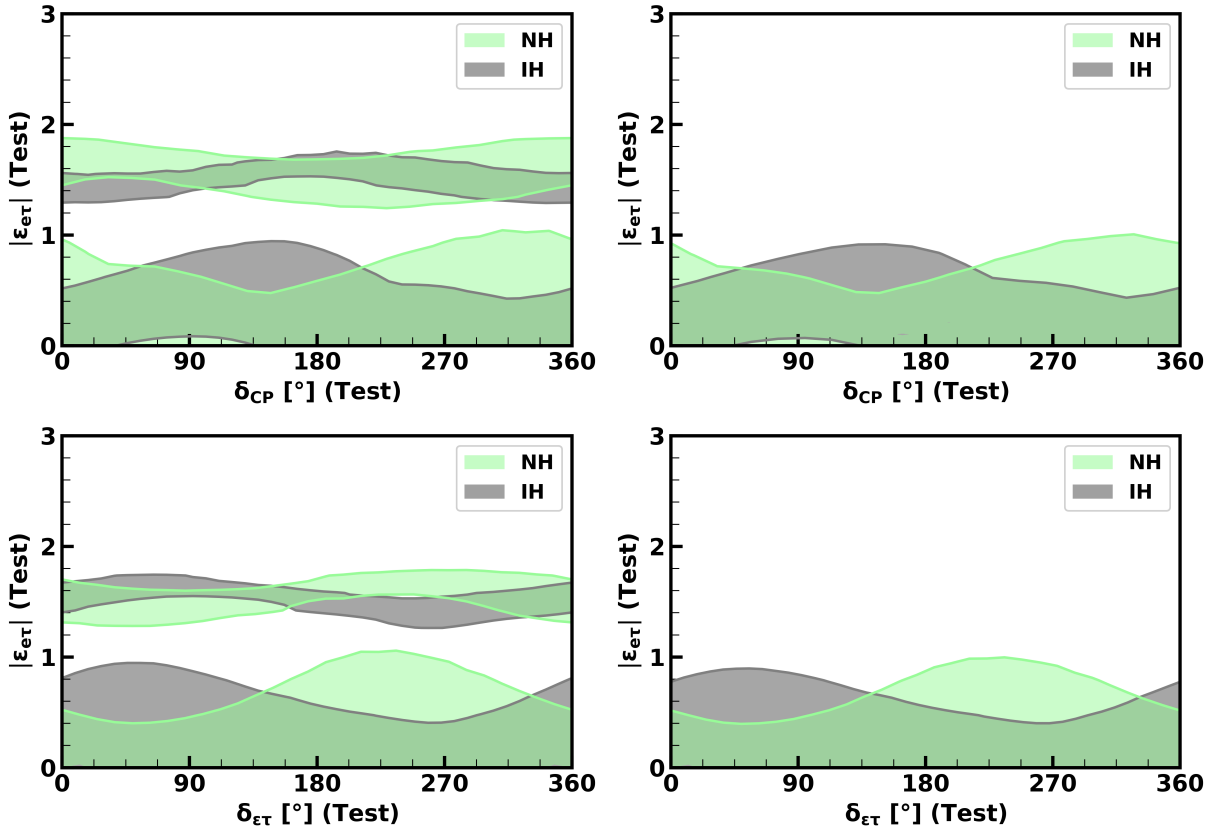


FIG. 2: $\epsilon_{e\tau}$ (test) vs δ_{CP} (test) in the upper row and $\epsilon_{e\tau}$ (test) vs $\delta_{e\tau}$ (test) in the lower row. In the left panel 1 - 4 GeV and in the right panel 1 - 20 GeV. Marginalized over θ_{13} , θ_{23} , Δm_{31}^2 , $\delta_{e\tau}$ (δ_{CP}) in upper row (lower row).

In the top-left plot of Fig. 2 we can see from the green bands (NH) that for each value of

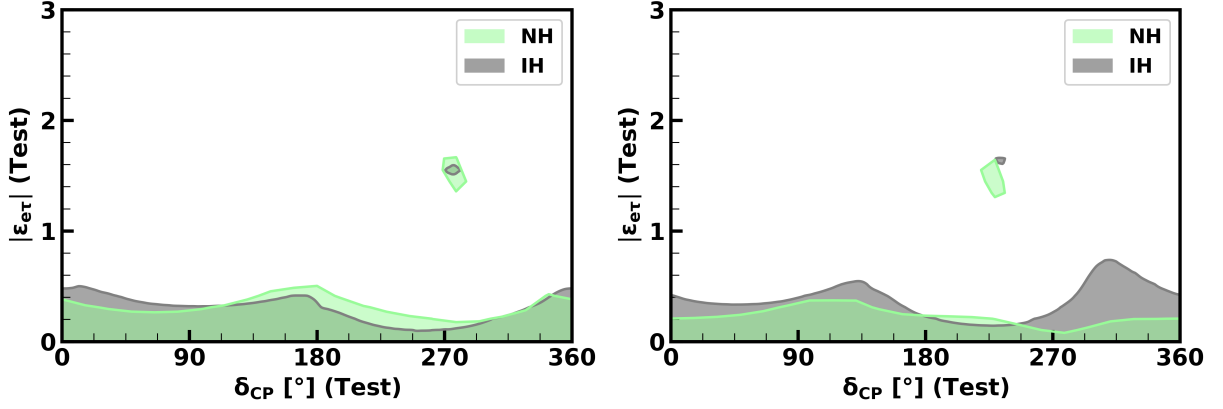


FIG. 3: $\epsilon_{e\tau}$ vs δ_{CP} for fixed $\delta_{e\tau} = 0$ in left and $\delta_{e\tau} = 45^\circ$ in right.

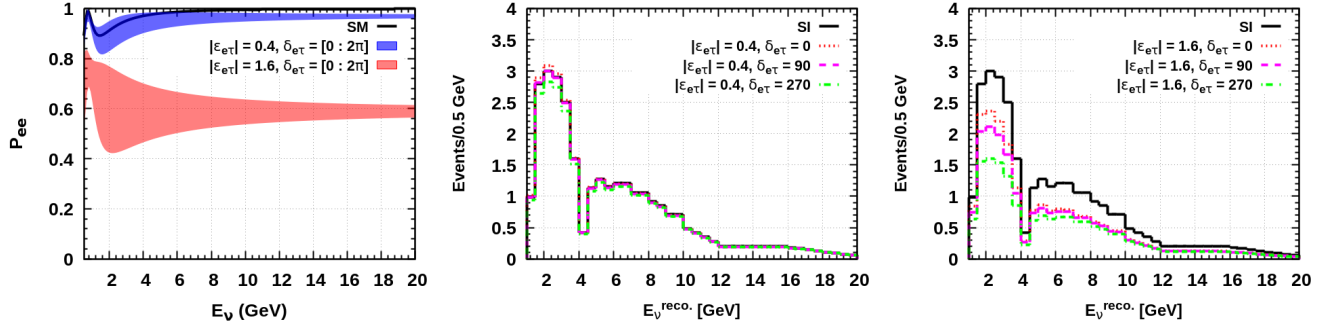


FIG. 4: P_{ee} vs energy (left) and beam background events per bin with reconstructed energy (middle and right). In the middle $|\epsilon_{e\tau}| = 0.4$ and in the right $|\epsilon_{e\tau}| = 1.6$. We show the plots for different $\delta_{e\tau} = 0, 90^\circ, 270^\circ$ in both the figures.

δ_{CP} , two bands span the allowed range in $\epsilon_{e\tau}$ parameter space indicating a degeneracy of the form $(\epsilon, \delta) = (\epsilon', \delta')$. Similar behavior is observed for the inverted hierarchy case and can be seen from the gray curve. These results agree with the results in ref. [12]. After including high-energy simulated events, plots shown in the right panel, we see the degeneracy in the $|\epsilon_{e\tau}|$ is removed for whole range of standard CP-phase δ_{CP} and corresponding non-standard phase $\delta_{e\tau}$. These observations are true for both the normal and inverted mass hierarchies. We investigate this further in the following.

Firstly to understand the degeneracy in the left panels of fig 2, we plot δ_{CP} vs $\epsilon_{e\tau}$ for fixed $\delta_{e\tau}$, $\delta_{e\tau} = 0$ in the left panel and $\delta_{e\tau} = 45^\circ$ in the right panel of fig. 3. From the left plot, we can see that there is a small degenerate region around $\epsilon_{e\tau} \sim 1.6$ corresponding to the $\delta_{CP} \sim 270^\circ$ for both

NH and IH bands. Similarly, in the right plot there is a degenerate region for $\epsilon_{e\tau} \sim 1.6$ around $\delta_{CP} \sim 225^\circ$ i.e. for $\delta_{CP} \sim (270 - 45)$. This can be generalized to the form $\delta_{CP} = 270 - \delta_{e\tau}$ or $3\pi/2$. This can be attributed to a degeneracy in the ν_e and $\bar{\nu}_e$ spectrum between SM and NSI ($\epsilon_{e\tau} \sim 1.6$, $\delta_{CP} = 270 - \delta_{e\tau}$). This agrees with the conclusions drawn in NOvA collaboration paper [11].

Further, we investigate the results obtained in the right panel of fig 2, where the degenerate bands around $\epsilon_{e\tau} \sim 1.6$ disappear. Here we are adding the high energy simulated events from $4 < E_\nu < 20$ GeV. Note that this high energy tail has both signal and background events contributing to the χ^2 as can be seen from fig. 1 (signal events) and fig. 4 (background events). Clearly, in comparison, the beam background is dominant compared to the signal events in this energy window. This can be verified from the $(4 - 20)$ GeV events given in the table II. To investigate the role of background in removing the degeneracy, we further look into the relevant oscillation channel P_{ee} . Therefore, we illustrate the probability vs E_ν (left panel) and events vs E_ν (assuming $\epsilon_{e\tau} = 0.4$ and $\epsilon_{e\tau} = 1.6$ in the middle and right panels) for the beam background channel $P(\nu_e \rightarrow \nu_e)$ in fig. 4. In all three plots, the relevant NSI parameters are as listed in the legends. In the left plot, the blue band (corresponding to $|\epsilon| = 0.4$ and $\delta_{e\tau} \in [0 : 2\pi]$) has a significant overlap with the SM curve (black curve) and, on the contrary, the red band (corresponding to $|\epsilon| = 1.6$ and $\delta_{e\tau} \in [0 : 2\pi]$) is well separated from the SM curve, indicating that the degeneracy between SM and NSI ($\epsilon_{e\tau} \sim 1.6$, $\delta_{CP} = 270 - \delta_{e\tau}$) can be broken when these events are considered in the analysis⁵. In the middle plot, the curves indicating different values of $\delta_{e\tau}$, $\epsilon_{e\tau} = 0.4$ are close to the SM curve (black) showing very less sensitivity to distinguish between SM and NSI. However, in the right panel the reasonable gap between the SM and NSI curves leads to the elimination of degeneracy in Fig. 2 (right panels).

Furthermore, the χ^2 analysis in Fig. 10 of the appendix A validates the role of beam background from high energy tail in removing the degeneracy $\epsilon_{e\tau} \sim 1.6$. We show 95% CL region in the $|\epsilon_{e\tau}|$ vs δ_{CP} ($\delta_{e\tau}$) plane in the left (right) plot considering only background (no signal) in the $4 < E_\nu < 20$ GeV energy window. We observe a narrow degeneracy band around $|\epsilon_{e\tau}| \sim 1.6$ in the left plot for the $\delta_{CP} \in [190^\circ : 270^\circ]$ in the case of NH. Other than that the degeneracy around $|\epsilon_{e\tau}| \sim 1.6$ is eliminated in both the left and right plots throughout the δ_{CP} and $\delta_{e\tau}$ range in case of both NH

⁵ We verified that in the case of signal probability $P_{\mu e}$ both the blue and red bands overlap with the SM curve $4 < E_\nu < 20$ GeV.

and IH. This observation infers that the background events from high energy tail contribute to eliminate the degeneracy, except the narrow band in the left plot for the $\delta_{CP} \in [190^\circ : 270^\circ]$ in the case of NH.

Signal events							
Hypothesis		$\nu_\mu \rightarrow \nu_e$			$\bar{\nu}_\mu \rightarrow \bar{\nu}_e$		
		1 - 4	1 - 20	4 - 20	1 - 4	1 - 20	4 - 20
		GeV	GeV	GeV	GeV	GeV	GeV
SM		59.0	61.0	2.0	19.0	19.6	0.6
$ \epsilon_{e\tau} = 0.4$	$\delta_{e\tau} = 0$	70.0	73	3.0	36.3	37.4	1.1
	$\delta_{e\tau} = \pi/2$	19.0	20.0	1.0	14.1	14.4	0.3
	$\delta_{e\tau} = 3\pi/2$	118.3	122.3	4.0	31.3	32.4	1.1
Beam background ($\nu_e + \bar{\nu}_e$)							
SM		13.7	29.6	15.9	7.6	16.4	8.8
$ \epsilon_{e\tau} = 0.4$	$\delta_{e\tau} = 0$	14.1	29.7	15.6	7.8	16.5	8.7
	$\delta_{e\tau} = \pi/2$	13.7	29.3	15.6	7.6	16.2	8.6
	$\delta_{e\tau} = 3\pi/2$	13.0	28.2	15.2	7.2	15.6	8.4
$ \epsilon_{e\tau} = 1.6$	$\delta_{e\tau} = 0$	10.6	20.9	10.3	5.9	11.6	5.7
	$\delta_{e\tau} = \pi/2$	9.5	19.4	9.9	5.3	10.7	5.4
	$\delta_{e\tau} = 3\pi/2$	7.5	16.3	8.8	4.1	9.0	4.9

TABLE II: Signal and background events at HE considering $\epsilon_{e\tau} \neq 0$.

D. Oscillation probabilities and event rates in the presence of $\epsilon_{e\mu}$

In this subsection, we illustrate the appearance probabilities and event rates w.r.t neutrino energy assuming non-zero $\epsilon_{e\mu}$. The approximate probability corresponding to $\nu_\mu \rightarrow \nu_e$ channel considering non-zero $\epsilon_{e\mu}$ is

$$\begin{aligned}
P_{\mu e} = & 2 \left[\frac{1}{\hat{A} - 1} \left\{ \frac{\eta s_{12} c_{12} s_{13} s_{23} c_{23}}{\hat{A}} + \eta s_{12} c_{12} s_{23}^2 c_{23} \epsilon_{e\mu} + s_{13} s_{23} c_{23}^2 \epsilon_{e\mu} + \hat{A} s_{23}^2 c_{23}^2 \epsilon_{e\mu}^2 \right\} \right. \\
& \times \left\{ -\cos\left(\frac{\Delta m_{21}^2 L}{2E}\right) - \cos\left(\frac{\Delta m_{31}^2 L}{2E}\right) + \cos\left(\frac{\Delta m_{32}^2 L}{2E}\right) + 1 \right\} \\
& - \frac{1}{\hat{A}^2} \left\{ \eta^2 s_{12}^2 c_{12}^2 c_{23}^2 + 2\eta \hat{A} s_{12} c_{12} c_{23}^3 \epsilon_{e\mu} + \hat{A}^2 c_{23}^4 \epsilon_{e\mu}^2 \right\} \left\{ \cos\left(\frac{\Delta m_{21}^2 L}{2E}\right) - 1 \right\} \\
& \left. - \frac{1}{(\hat{A} - 1)^2} \left\{ s_{13}^2 s_{23}^2 + 2\hat{A} s_{13} s_{23}^3 \epsilon_{e\mu} + \hat{A}^2 s_{23}^4 \epsilon_{e\mu}^2 \right\} \left\{ \cos\left(\frac{\Delta m_{31}^2 L}{2E}\right) - 1 \right\} \right]. \quad (3.7)
\end{aligned}$$

In the left panel of fig. 5 we show ν_e (upper) and $\bar{\nu}_e$ (lower) numerical appearance probabilities using eq. (3.4). In each of the probability plots we draw five curves; the black curve represents standard oscillation probability, the blue band depicts the resultant probability for $|\epsilon_{e\mu}| = 0.3$ and $\delta_{e\mu} \in [0 : 2\pi]$, the red dotted, magenta dashed and green dot-dashed curves stand for nonstandard phases $\delta_{e\mu} = 0$, $\delta_{e\mu} = \pi/2$ and $\delta_{e\mu} = 3\pi/2$ respectively. In all the plots we assume NH as the true mass hierarchy.

From the left panel of fig. 5 the blue band corresponding to non-zero $|\epsilon_{e\mu}| = 0.3$ and $\delta_{e\mu} \in [0 : 2\pi]$ spans a wide range of probability values both greater and lesser than the standard oscillation probability (black curve). Whereas for $E_\nu > 7$ GeV, we do not observe degeneracy for the chosen parameters; rather, we see the increase in probabilities w.r.t standard oscillation. Additionally, we show the curves corresponding to CP conserving ($\delta_{e\mu} = 0$) and maximal CP violation ($\delta_{e\mu} = \pi/2, 3\pi/2$) using red, magenta and blue lines respectively.

In the middle and right panels we depict event rates as a function of reconstructed energy ranging from $1 < E_\nu < 4$ GeV and $4 < E_\nu < 20$ GeV respectively. The top and bottom panels correspond to ν_e and $\bar{\nu}_e$ appearance channels respectively. The relevant legends are listed within each plot. The ν_e and $\bar{\nu}_e$ appearance channels in the middle panel depict the event rates considered by the NOvA collaboration in ref. [11]. In the right most panel we show signal events corresponding to $E_\nu : 4 - 20$ GeV both for SM and assuming non-zero $\epsilon_{e\mu}$. The trends followed by events spectra

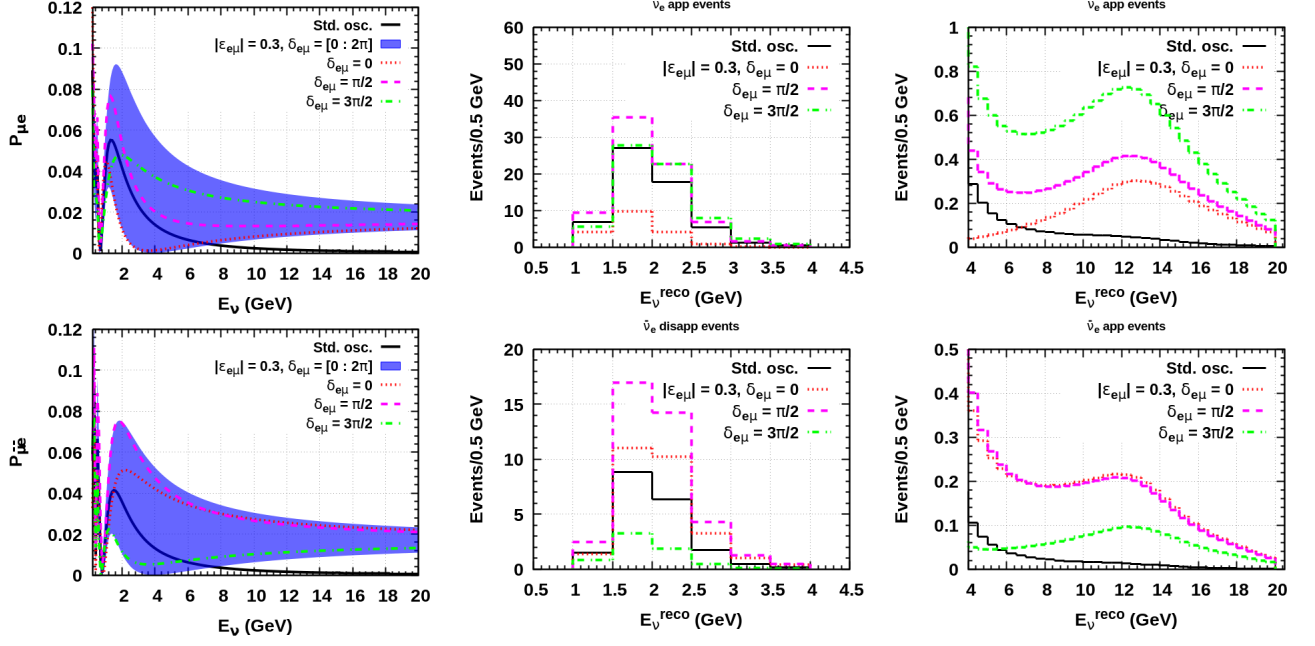


FIG. 5: Appearance probability versus neutrino energy and event rates versus reconstructed energy for ν_e ($\bar{\nu}_e$) in the upper (lower) row. We consider $|\epsilon_{e\mu}| = 0.3$ and corresponding phases to show modified probability and event rates in the presence of non-standard interaction.

in these panels are easily understandable from the corresponding probability plots of the left most panels.

E. Allowed regions in $\epsilon_{e\mu}$ and $\delta_{CP(e\mu)}$ parameter space

In fig. 6 we show 2-dimensional sensitivity analysis by projecting χ^2 in $|\epsilon_{e\mu}|(test) - \delta_{CP}(test)$ plane (upper row) and $|\epsilon_{e\mu}|(test) - \delta_{e\mu}(test)$ plane (lower row). We plot the contours in the left and right panels considering simulated NOvA events for standard framework ($1 < E_\nu < 4$ GeV) and including high energy ($1 < E_\nu < 20$ GeV), respectively. We calculate $\Delta\chi^2$ hypothesizing standard oscillation in the true simulated data and NSI in the theory and plot 95% CL contour in the $\epsilon_{e\mu}[test]$ versus $\delta_{CP}[test]$ plane. We define the $\Delta\chi^2$ as

$$\Delta\chi^2 = \chi^2(\epsilon_{e\mu}[true] = 0, \epsilon_{e\mu}[test] \neq 0), \quad (3.8)$$

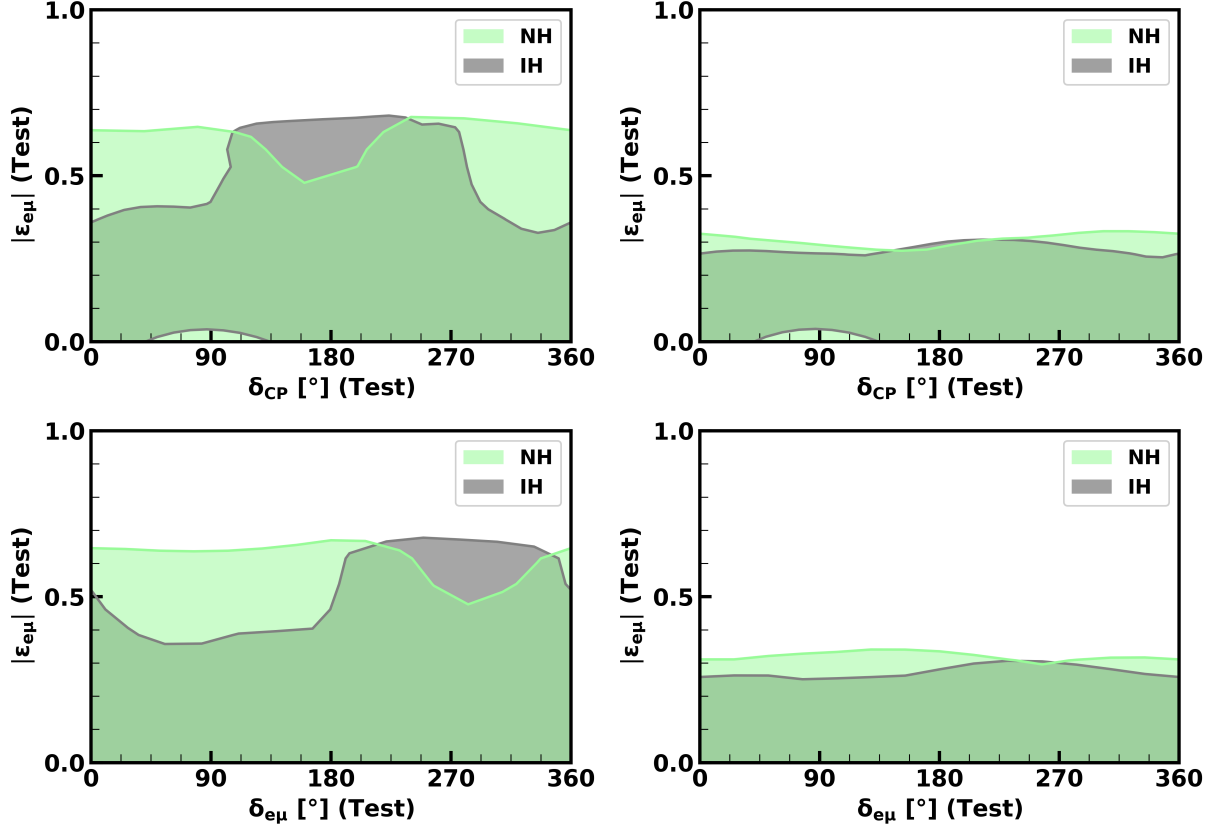


FIG. 6: $\epsilon_{e\mu}$ (test) vs δ_{CP} (test) in the upper row and $\epsilon_{e\mu}$ (test) vs $\delta_{e\mu}$ in the lower row. In the left panel 1 - 5 GeV and in the right panel 1 - 20 GeV. Marginalized over θ_{13} , θ_{23} , Δm_{31}^2 , $\delta_{e\mu}$ (δ_{CP}) in upper row (lower row).

for the fix true δ_{CP} at 0.82π and marginalize over θ_{13} , θ_{23} , Δm_{31}^2 and $\delta_{e\mu}$. Similarly, we calculate $\Delta\chi^2$ using eq. 3.8 corresponding to $\epsilon_{e\mu}[\text{test}]$ versus $\delta_{e\mu}[\text{test}]$ contour, where we marginalize over θ_{13} , θ_{23} , Δm_{31}^2 and δ_{CP} . We vary δ_{CP} and $\delta_{e\mu}$ in their full range $0 - 2\pi$ and show contours with 95% CL for both the normal hierarchy (NH, green regions) and inverted hierarchy (IH, gray region). The unmentioned oscillation parameters are kept fixed to their true values. Note that NOvA disfavors the region above the gray line for NH and green line for IH.

From the top-left plot, considering NH, we observe the allowed region (with 95% CL) favors relatively lower $|\epsilon_{e\mu}|$ in the $\delta_{CP} \sim [90^\circ : 220^\circ]$, whereas the contour favors higher $\epsilon_{e\mu}$ elsewhere. For IH, the contour encompasses relatively higher $|\epsilon_{e\mu}|$ in the $\delta_{CP} \sim [90^\circ : 270^\circ]$, while it adopts lower $\epsilon_{e\mu}$ elsewhere. In the bottom-left plot, considering NH (IH), the 95% CL contour favors relatively

lower (higher) $|\epsilon_{e\mu}|$ in the $\delta_{e\mu} \sim [220^\circ : 340^\circ]$ ($[180^\circ : 360^\circ]$). The range of $\epsilon_{e\mu}$ corresponding to allowed contours are identical in both the upper and lower plots as well as for NH and IH. This implies that the sensitivity to $\epsilon_{e\mu}$ remains almost unchanged w.r.t δ_{CP} or $\delta_{e\mu}$ and irrespective of mass hierarchy. A noteworthy fact is that the contours favor relatively lower $\epsilon_{e\mu}$ in the presence of high energy events for both the plots in the right panel. This indicates, including high energy events provides better constraints on $\epsilon_{e\mu}$.

IV. Study of environmental decoherence including $\nu_e/\bar{\nu}_e$ high energy events

Neutrino oscillation data from the experiments rely on the three flavor mixing where the propagation of neutrinos is interpreted as the coherent superposition of mass eigenstates. In this quantum evolution the degree of coherence remains unaffected over the macroscopic distances because of the weak coupling of neutrinos with matter. Such phenomenon manifests the isolation of neutrino systems from their surroundings while propagation. Nevertheless, neutrinos could interact with the stochastic environment [32], for instance fluctuating space-time at the Planck scale, matter density fluctuation, virtual black hole. This incorporates the loss of coherence in propagating neutrinos states and introduces a non-standard effect which is known as environmental decoherence⁶. In this phenomenology we assume neutrino (sub-)system is an open quantum system and interacts with the environment. In the presence of environmental interaction the neutrino oscillation probability gets modified and carries damping term $e^{-\Gamma L}$, where Γ is the decoherence parameter. Γ could depend on the different power of the neutrino energy as $\Gamma \propto E^n$, here choice of n is based on the various physical origins of decoherence phenomenon.

A. Mathematical formulation of oscillation probabilities

Neutrino propagation in an open quantum system framework introduces loss of coherence due to interaction of neutrino subsystem with the stochastic environment. This loss is incorporated using Lindblad master equation which represents the density matrix evolution as given below [38, 39]

$$\frac{d\rho^m(t)}{dt} = -i[H, \rho^m(t)] + \mathcal{D}[\rho^m(t)], \quad (4.1)$$

⁶ This effect is different from neutrino wave-packet decoherence [33–37]

where ρ_m is the density matrix of neutrino states in the mass basis and H is the Hamiltonian of the neutrino system. The damping term $\mathcal{D}[\rho_m(t)]$ represents the interaction neutrino system and the environment. The parameterization of $\mathcal{D}[\rho_m(t)]$ is obtained by using complete positivity and trace preserving conditions. Applying complete positivity modifies the Lindblad form of the dissipator as [40]

$$\mathcal{D}[\rho^m(t)] = \frac{1}{2} \sum_{n=1}^{N^2-1} \{[\mathcal{V}_n, \rho^m \mathcal{V}_n^\dagger] + [\mathcal{V}_n \rho^m, \mathcal{V}_n^\dagger]\}, \quad (4.2)$$

here N is the dimension of the Hilbert space and \mathcal{V}_n are the interaction operators. Further, we impose an increase in von Neumann entropy $S = -Tr(\rho^m \ln \rho^m)$ [41, 42] and conservation of average energy $Tr(\rho^m H)$ of the neutrino system and obtain the elements of time evolved density matrix,

$$\begin{aligned} \rho_{jk}^m(t) &= \rho_{jk}(0), \text{ for } j = k, \\ \rho_{jk}^m(t) &= \rho_{jk}(0) \exp -(\Gamma_{jk} + i\Delta_{jk}), \text{ for } j \neq k. \end{aligned} \quad (4.3)$$

with

$$\Gamma_{jk} = \Gamma_{kj} = \frac{1}{2} \sum_{n=1}^8 (d_{n,j} - d_{n,k})^2, \quad (4.4)$$

where, $d_{n,j}$, $d_{n,k}$ are the diagonal elements of \mathcal{V}_n operator and j, k take the values 1, 2, 3.

We consider the modified-mixing matrix (\tilde{U}) up to the 1st order approximation, from ref. [43] to convert mass basis to flavor basis using $\tilde{\rho}^\alpha = \tilde{U} \tilde{\rho}^m \tilde{U}^\dagger$. The neutrino transition probability from initial flavor ' ν_α ' to final flavor ' ν_β ' in terms of density matrix is obtained by

$$P_{\alpha\beta}(t) = Tr[\tilde{\rho}_\alpha(t) \tilde{\rho}_\beta(0)]. \quad (4.5)$$

The explicit form of the transition probability assuming ultra-relativistic neutrinos ($t \approx L$) is given by [44, 45]

$$\begin{aligned} P_{\alpha\beta}(L) &= \delta_{\alpha\beta} - 2 \sum_{j>k} Re \left(\tilde{U}_{\beta j} \tilde{U}_{\alpha j}^* \tilde{U}_{\alpha k} \tilde{U}_{\beta k}^* \right) + 2 \sum_{j>k} Re \left(\tilde{U}_{\beta j} \tilde{U}_{\alpha j}^* \tilde{U}_{\alpha k} \tilde{U}_{\beta k}^* \right) \exp(-\Gamma_{jk}L) \cos \left(\frac{\tilde{\Delta}m_{jk}^2}{2E} L \right) \\ &\quad + 2 \sum_{j>k} Im \left(\tilde{U}_{\beta j} \tilde{U}_{\alpha j}^* \tilde{U}_{\alpha k} \tilde{U}_{\beta k}^* \right) \exp(-\Gamma_{jk}L) \sin \left(\frac{\tilde{\Delta}m_{jk}^2}{2E} L \right). \end{aligned} \quad (4.6)$$

Here in eq. (4.6), the term $e^{-\Gamma_{jk}L}$ damps the oscillation probability. We analyze the effect of decoherence by considering all the Γ_{jk} as equal (i.e., $\Gamma_{21} = \Gamma_{31} = \Gamma_{32}$) and represent it by a single

parameter Γ for simplicity. Further we assume a general power law dependency of Γ parameter on the neutrino energy given by

$$\Gamma(E_\nu) = \Gamma_0 \left(\frac{E_\nu}{E_0} \right)^n, \quad (4.7)$$

where, Γ_0 is constant, E_0 is the reference energy taken as 1 GeV and $n = 0, \pm 1, \pm 2$. Different physical origins explain the decoherence phenomena leading to different integral power law dependencies [46]. However, from eq. (4.7) one can note that the oscillation probabilities are sensitive to $n > 0$ when $E_\nu > E_0$. In case of NOvA experiment $E_\nu \sim 1.8$ GeV is greater than the reference energy (1 GeV), so environmental decoherence plays significant role when $n > 0$ and which could yield stronger constraints on Γ .

It is noteworthy to mention that, the neutrino oscillation probabilities are sensitive to positive powers of n (leftmost panel of fig. 7). This happens because the energy of the neutrino beam E_ν is greater than the reference energy $E_0 = 1$ GeV ($E_\nu \geq E_0$) in eq. 4.7.

The analytical appearance and disappearance probabilities considering perturbative expansion up to the first order in small parameters s_{13} and η are shown below

$$\begin{aligned} P_{\mu e} = & \frac{2}{\hat{A} - 1} \left[\frac{\eta s_{12} c_{12} s_{13} s_{23} c_{23}}{\hat{A}} \left\{ -e^{-\Gamma_{21}L} \cos\left(\frac{\Delta m_{21}^2 L}{2E}\right) - e^{-\Gamma_{31}L} \cos\left(\frac{\Delta m_{31}^2 L}{2E}\right) \right. \right. \\ & \left. \left. + e^{-\Gamma_{32}L} \cos\left(\frac{\Delta m_{32}^2 L}{2E}\right) + 1 \right\} - \frac{\hat{A} - 1}{\hat{A}^2} \eta^2 s_{12}^2 c_{12}^2 c_{23}^2 \left\{ e^{-\Gamma_{21}L} \cos\left(\frac{\Delta m_{21}^2 L}{2E}\right) - 1 \right\} \right. \\ & \left. - \frac{s_{13}^2 s_{23}^2}{\hat{A} - 1} \left\{ e^{-\Gamma_{31}L} \cos\left(\frac{\Delta m_{31}^2 L}{2E}\right) - 1 \right\} \right], \end{aligned} \quad (4.8)$$

and

$$\begin{aligned} P_{\mu\mu} = & 1 + 2 \left[\frac{c_{23}^2}{\hat{A}^2} \eta^2 s_{12}^2 c_{12}^2 + \frac{2c_{23}s_{23}}{\hat{A}(\hat{A} - 1)} \eta s_{12} c_{12} s_{13} + c_{23}^2 s_{23}^2 \left\{ e^{-\Gamma_{32}L} \cos\left(\frac{\Delta m_{32}^2 L}{2E}\right) - 1 \right\} \right. \\ & \left. + \frac{s_{23}^2}{(\hat{A} - 1)^2} s_{13}^2 \left\{ c_{23}^2 e^{-\Gamma_{21}L} \cos\left(\frac{\Delta m_{21}^2 L}{2E}\right) + s_{23}^2 e^{-\Gamma_{31}L} \cos\left(\frac{\Delta m_{31}^2 L}{2E}\right) - 1 \right\} \right]. \end{aligned} \quad (4.9)$$

B. Oscillation probabilities and event rates

We show the oscillation probability in the presence of decoherence effect (using eq. (4.6)) to demonstrate the deviation as compared to standard three flavor scenarios. In the top row of fig. 7

we depict ν_e -appearance probability and corresponding event rates, and in the bottom row ν_μ -disappearance probability and corresponding event rates. In the left panel we show probabilities as a function of energy. In the middle and right panels we illustrate event rates as a function of reconstructed energy correspond to $1 < E_\nu < 4$ GeV and $4 < E_\nu < 20$ GeV, respectively. We compute the probabilities and event rates numerically considering standard parameters from table I and assuming decoherence parameter $\Gamma = 10^{-23}$ GeV along with the energy power-law dependencies. In each plot we display the curves corresponding to the standard oscillation and decoherence with power-law indices $n = 0, \pm 1, \pm 2$ as per their respective legends shown in the plots. We tabulate the event rates for all the mentioned cases in table III.

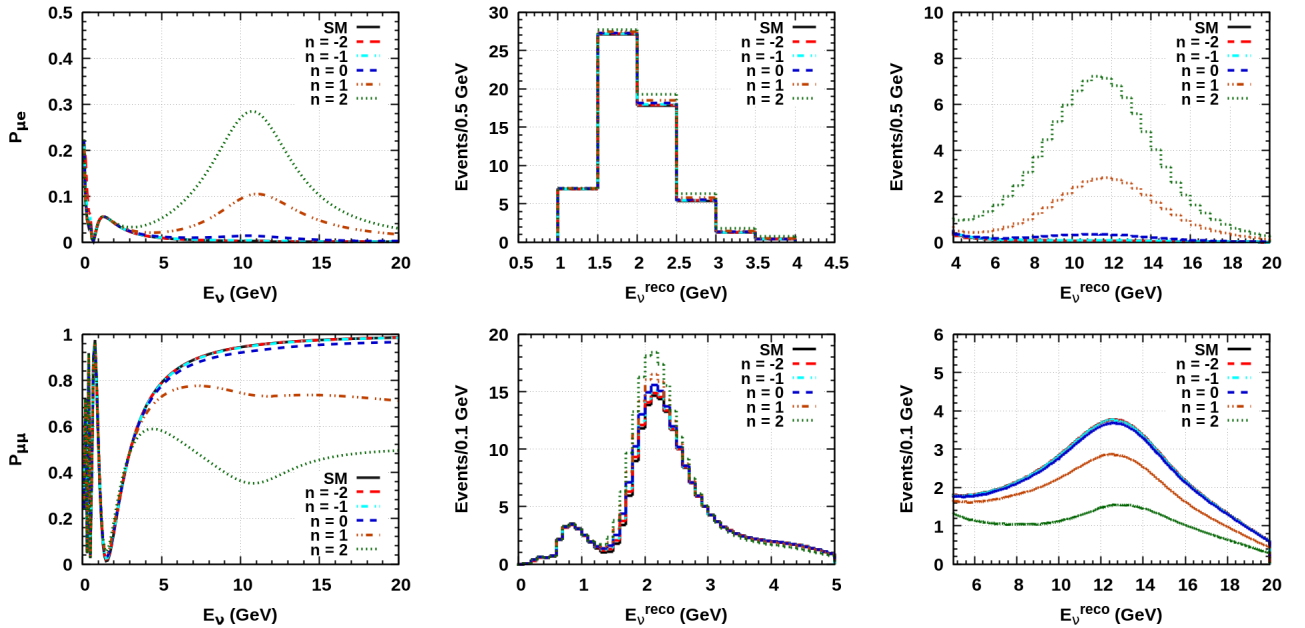


FIG. 7: ν_e appearance probability and event rates in the top row. ν_μ disappearance probability and event events in the bottom row. We assume $\Gamma = 10^{-23}$ GeV.

From the left plots we observe a marginal impact of decoherence on the oscillation probabilities in the energy range $1 < E_\nu < 4$ GeV. Adopting power-law indices $n = -2, -1$ (red, cyan curves) we notice negligible effect of Γ on the appearance and disappearance channels in the energy window $4 < E_\nu < 20$ GeV. For $n = 0$ (blue) we see the effect of decoherence is less prominent, whereas $n = 1, 2$ lead to a noticeable impact on both the appearance and disappearance probabilities. Additionally ~ 11 GeV we see an increase in $\nu_\mu \rightarrow \nu_e$ probability (top left) and decrease in

Signal events							
Channel		$\nu_\mu \rightarrow \nu_e$			$\nu_\mu \rightarrow \nu_\mu$		
Energy range (GeV)		1 – 4	1 – 20	4 – 20	1 – 4	1 – 20	4 – 20
SM		59.0	61.0	2.0	215.0	589.8	374.8
$\Gamma_0 = 10^{-23}$ GeV	$n = -2$	59.1	61.2	2.1	218.0	592.7	374.7
	$n = -1$	59.3	61.7	2.4	220.8	594.9	374.1
	$n = 0$	59.7	66.0	6.3	225.9	592.3	366.4
	$n = 1$	60.7	101.0	40.3	234.8	529.8	295.0
	$n = 2$	63.0	165.9	102.9	250.1	423.8	173.7

TABLE III: Excess number of events in HE ($4 < E_\nu < 20$ GeV) considering $\Gamma \neq 0$.

$\nu_\mu \rightarrow \nu_\mu$ (bottom left) as compared to the corresponding standard oscillation scenario. From these plots we observe that the neutrino oscillation probabilities deviate from the SM case for $n > 0$. This is the consequence of the power-law in eq. (4.7), since our analysis includes neutrino energy higher than the reference energy i.e., ($E_0 = 1$ GeV). The details of the peak that arises around ~ 11 GeV have been discussed in ref. [47]. The event rates in the middle and right panels also follow a similar trend as the oscillation probabilities. For power-law indices $n = 0, 1, 2$ ⁷ considering HE events could provide better constraints on Γ .

C. Upper bounds on the decoherence parameter Γ

To obtain the upper bounds on Γ_0 we show the 2-dimensional χ^2 distribution in the test Γ_0 versus true δ_{CP} plane considering power-law indices $n = 0, 1, 2$. Here we are not showing the corresponding plots for $n = -2, -1$ as the effect of Γ on $P_{\mu e}$ and $P_{\mu\mu}$ is negligible as seen in fig. 7. We compute the χ^2 values for every true $\delta_{CP} \in [0, 360^\circ]$ by assuming the standard oscillation phenomenon in the

⁷ Energy independent decoherence when $n = 0$, whereas $n = 1$ refers to the linear energy dependence that could be modeled from *foamy* fluctuations in space-time [48], and $n = 2$ leads to the quadratic energy dependency on Γ could be induced by quantum gravity effect [49].

simulated data and the decoherence scenario in the theory. We provide the definition of χ^2 below

$$\chi_{\Gamma}^2(\delta_{CP}^{true}) = \chi^2(\Gamma^{true} = 0, \Gamma^{test} \neq 0) , \quad (4.10)$$

and marginalize over test parameters δ_{CP} , θ_{23} , Δm_{31}^2 .

In fig. 8 the left, right and middle plots represent the results for $n = 0$, $n = 1$ and $n = 2$ respectively. In each of these plots the solid lines depict the χ^2 obtained for the energy range $E_\nu : 1 - 4$ GeV while the dashed lines show the results for $E_\nu : 1 - 20$ GeV. The blue and red curves stand for 90% and 95% CL respectively.

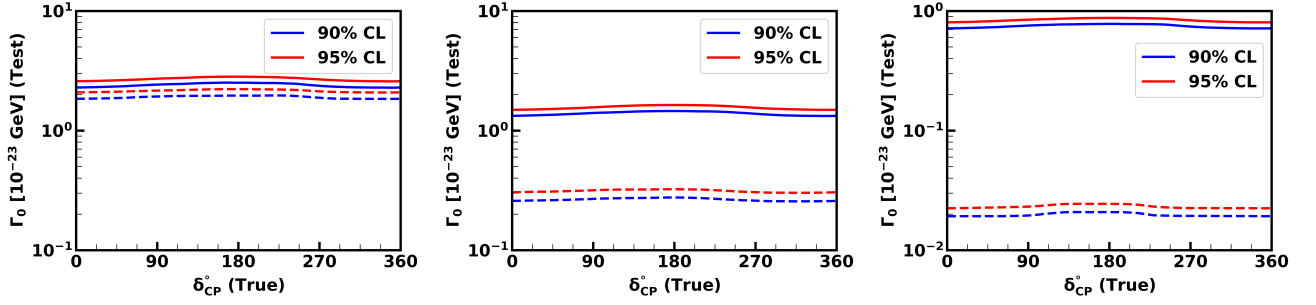


FIG. 8: Constraining Γ_0 using energy range $1 - 4$ GeV (solid lines) and $1 - 20$ GeV (dashed lines). Left, middle and right plots correspond to $n = 0$, $n = 1$ and $n = 2$ respectively. We marginalize over Δm_{31}^2 , θ_{23} , δ_{CP} .

Across all the plots we point out from the solid and dashed curves that including high energy events ($E_\nu : 1 - 20$ GeV) provide comparatively better constraint on Γ_{jk} than NOvA standard analysis window $E_\nu : 1 - 4$ GeV. However, this confirmation is less significant assuming $n = 0$ (left) and dominate with increasing n ($= 1, 2$; middle, right plots). We can explain such behavior from the ν_e -appearance probability and corresponding event rates in fig. 7. In all the plots we see that 90% (blue) and 95% CL (red) curves are closer to each other therefore we list the bounds corresponding to 90% CL in this section. We also notice that the corresponding bounds on Γ remain almost constant (as blue curves are flat) for all values of δ_{CP} . This indicates that the decoherence parameter Γ does not depend on the true value of δ_{CP} .

Considering $E_\nu : 1 - 4$ GeV the sensitivity at 90% CL to the Γ_0 for $n = 0, 1, 2$ is listed as 2.2×10^{-23} GeV, 1.3×10^{-23} GeV, 7.15×10^{-24} GeV respectively. Whereas analyzing events from $E_\nu : 1 - 20$ GeV the sensitivity at 90% CL to the Γ_0 for $n = 0, 1, 2$ is listed as 1.82×10^{-23} GeV,

Analysis window	Bounds on Γ_0 (GeV)		
	$n = 0$	$n = 1$	$n = 2$
$E_\nu : 1 - 4$ GeV	2.2×10^{-23}	1.3×10^{-23}	7.15×10^{-24}
$E_\nu : 1 - 20$ GeV	1.82×10^{-23}	2.52×10^{-24}	2.0×10^{-25}

TABLE IV: Bounds on Γ_0 obtained from fig 8 for different power-law indices $n = 0, 1, 2$.

2.52×10^{-24} GeV, 2.0×10^{-25} GeV respectively. Clearly, for $n = 1, 2$ we note more stringent bounds (by $\mathcal{O}(1)$) when we added high energy events from $E_\nu : 4 - 20$ GeV. Notably, in the case of $n = 2$ (right most plot) we see a significant improvement in the bounds of Γ in comparison to the results obtained from assuming $E_\nu : 1 - 4$ GeV and this can be observed from solid and dashed curves. To facilitate a better comparison we list all the bounds in the table IV.

D. Allowed regions in θ_{23} - δ_{CP} plane

In this sub-section we choose to highlight the most stringent bounds on θ_{23} and δ_{CP} imposed by assuming non-zero Γ with a power-law index $n = 2$. We achieve this by assuming decoherence in both the simulated data and the test hypothesis. To obtain the the projection of χ^2 in then $\theta_{23} - \delta_{CP}$ test plane we define χ^2 as follows

$$\chi^2 = \chi^2(\Gamma^{true}, \delta_{CP}^{true}, \theta_{23}^{true}, \delta_{CP}^{test}, \theta_{23}^{test}) . \quad (4.11)$$

We marginalize over test Δm_{31}^2 , θ_{13} and Γ [$10^{-24} : 10^{-22}$] GeV. We consider true values of standard parameters and their test ranges from table I assuming normal mass ordering. We fix the unmentioned parameters to their true values.

In fig. 9 we display the projection of χ^2 in the test plane of $\theta_{23} - \delta_{CP}$ plane considering true $\Gamma_0 = 10^{-23}$ GeV (a representative value) and energy power-law indices $n = 0, 1$ and 2 in the top, middle and bottom panel. The left and right plots represent allowed regions considering analysis window of neutrino energy 1 to 4 GeV and 1 to 20 GeV respectively. In both the plots we show the contours corresponding to 68% (gray) and 90% (blue) CL.

From the left plot of fig. 9 ($E_\nu : 1 - 4$ GeV) we notice that even in the presence of decoherence

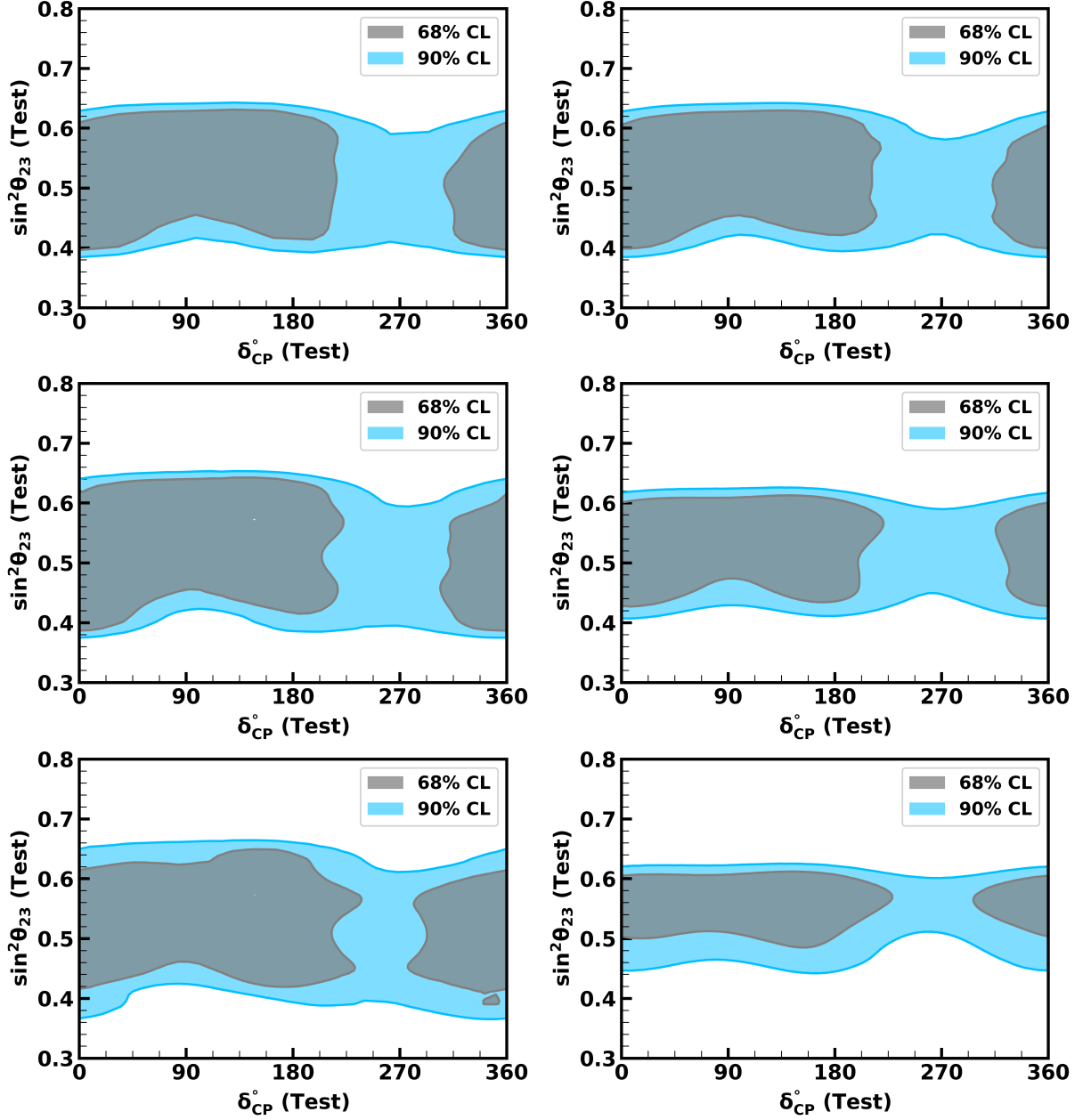


FIG. 9: $\Gamma_{21} = \Gamma_{31} = \Gamma_{32} = 10^{-23}$ GeV in true for $n = 0$ in top row, $n = 1$ in middle row and $n = 2$ in bottom row

. In left 1 - 5 GeV and in right 1 - 20 GeV. Marginalized over Δm_{31}^2 , θ_{13} and Γ

the allowed regions of θ_{23} and δ_{CP} are almost the same as in the standard case reported in [8]. This implies that when we consider the ν_e events in the range $E_\nu : 1 - 4$ GeV the impact of the presence of decoherence, in true spectrum is very minimal (even for power law index $n = 2$). On

the contrary, when we considered $E_\nu : 4 - 20$ GeV (right panel), we note that the allowed regions of θ_{23} for all values of δ_{CP} got more stringent for $n = 1, 2$ and the higher octant of θ_{23} ($\theta_{23} > 45^\circ$) is preferred over the lower octant ($\theta_{23} < 45^\circ$) for $n = 2$.

Furthermore, we observe a disfavor region for $\delta_{CP} \sim 270^\circ$ with 68% CL in both the left and right plots even in the presence of decoherence and the region is allowed with 90% CL. Therefore, in the presence of decoherence the NOvA and T2K tension shown in ref. [8] (normal ordering plot in fig. 6), could be uplifted with 90% CL.

V. Conclusions

In this paper we have studied the phenomenology of NSI and environmental decoherence by including high energy neutrino events at NOvA experiment. We have shown the modified oscillation probabilities and event rates at high energy considering effect of one NSI parameters ($\epsilon_{e\mu}$, $\epsilon_{e\tau}$ at a time) as well as decoherence parameter Γ . We have illustrated the allowed regions with 95% CL in the $|\epsilon_{\alpha\beta}| - \delta_{CP(\alpha\beta)}$ plane taking into account high energy ν_e and $\bar{\nu}_e$ events. We have obtained the bounds on decoherence parameter Γ considering the power-law dependencies $n = 0, 1, 2$. In the decoherence scenario we have highlighted the bounds on θ_{23} and δ_{CP} imposed by assuming power-law indices $n = 0, 1, 2$ for the analysis window $E_\nu : 1 - 20$ GeV.

The standard appearance probability and the probability with non-zero $\epsilon_{e\tau}$ exhibit the degeneracy throughout the energy window considered in this analysis. Interestingly, the degeneracy observed for higher $\epsilon_{e\tau}$ in the $|\epsilon_{e\tau}| - \delta_{CP(e\tau)}$ plane disappears if we include events from high energy range ($E_\nu : 4 - 20$ GeV). On the other hand the appearance probability increases at high energy ($E_\nu > 7$ GeV) as compared to standard oscillation probability in the presence of $\epsilon_{e\mu}$ and we do not observe degeneracy with the standard oscillation probability. In addition, the 95% CL contours in $|\epsilon_{e\mu}| - \delta_{CP(e\mu)}$ plane show that $\epsilon_{e\mu}$ can be tightly constrained for all values of δ_{CP} after including high energy events.

In the case of decoherence we have seen an increase in ν_e -appearance probability and events ~ 11 GeV for $n \geq 0$. Including the high energy events we have obtained stringent upper bounds on Γ specifically for power-law indices $n = 1, 2$. Considering non-zero Γ with $n = 2$, we have shown that θ_{23} is better constrained for all values of δ_{CP} and the higher octant of θ_{23} ($\theta_{23} > 45^\circ$)

is preferred over the lower octant ($\theta_{23} < 45^\circ$) including events from $E_\nu : 4 - 20$ GeV.

Acknowledgments

We would like to thank Prof. Mark Messier and Prof. Jon Urheim, Indiana University, USA, for their continuous assistance and valuable support with this work. Special thanks to Ishwar Singh, University of Delhi, for fruitful discussions. One of the authors (K. N. D.) acknowledges the Department of Science and Technology (DST)-SERB International Research Experience (SIRE) program for the financial support Grant No. SIR/2022/000518 to visit Indiana University, USA. We acknowledge high performance computing (HPC) facilities in École Centrale School of Engineering - Mahindra University.

A. $\epsilon_{e\tau}$ vs δ_{CP} ($\delta_{e\tau}$) assuming no signal in $E_\nu : 5 - 20$ GeV

In fig. 10, we consider simulated data from $E_\nu : 1 - 4$ GeV accompany signal and background, whereas $E_\nu : 4 - 20$ GeV spectra accompany only background.

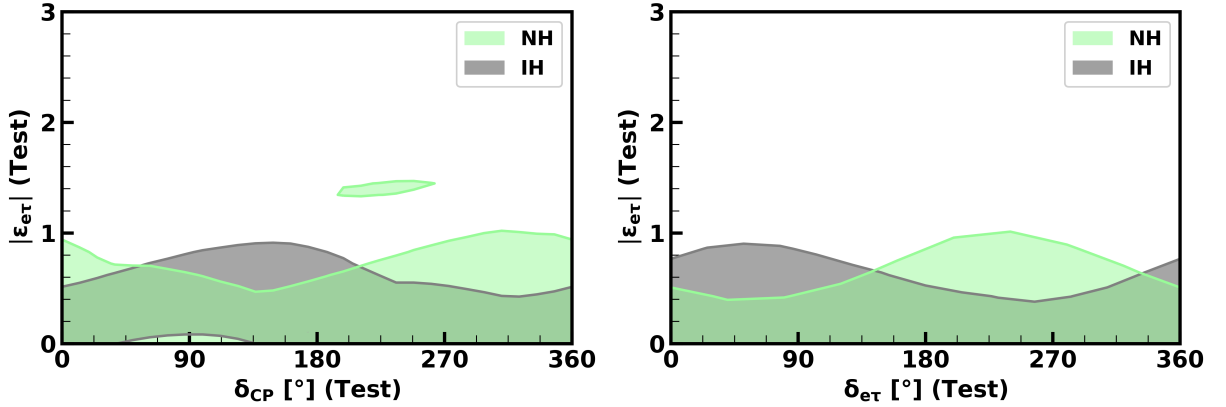


FIG. 10: $\epsilon_{e\tau}$ vs δ_{CP} (left) and $\epsilon_{e\tau}$ vs $\delta_{e\tau}$ (right) for only background (no signal) in energy range $E_\nu : 5 - 20$ GeV.

-
- [1] L. Wolfenstein, Neutrino Oscillations in Matter, Phys. Rev. D 17 (1978) 2369–2374. [doi:10.1103/PhysRevD.17.2369](https://doi.org/10.1103/PhysRevD.17.2369).

- [2] E. Roulet, MSW effect with flavor changing neutrino interactions, Phys. Rev. D 44 (1991) R935–R938. [doi:10.1103/PhysRevD.44.R935](#).
- [3] T. Hattori, T. Hasuike, S. Wakaizumi, Flavor changing neutrino interactions and CP violation in neutrino oscillations, Prog. Theor. Phys. 114 (2005) 439–449. [arXiv:hep-ph/0210138](#), [doi:10.1143/PTP.114.439](#).
- [4] C.-H. Chang, W.-S. Dai, X.-Q. Li, Y. Liu, F.-C. Ma, Z.-j. Tao, Possible effects of quantum mechanics violation induced by certain quantum gravity on neutrino oscillations, Phys. Rev. D 60 (1999) 033006. [arXiv:hep-ph/9809371](#), [doi:10.1103/PhysRevD.60.033006](#).
- [5] F. Benatti, R. Floreanini, Open system approach to neutrino oscillations, JHEP 02 (2000) 032. [arXiv:hep-ph/0002221](#), [doi:10.1088/1126-6708/2000/02/032](#).
- [6] Y. Farzan, T. Schwetz, A. Y. Smirnov, Reconciling results of LSND, MiniBooNE and other experiments with soft decoherence, JHEP 07 (2008) 067. [arXiv:0805.2098](#), [doi:10.1088/1126-6708/2008/07/067](#).
- [7] P. B. Denton, J. Gehrlein, R. Pestes, CP -Violating Neutrino Nonstandard Interactions in Long-Baseline-Accelerator Data, Phys. Rev. Lett. 126 (5) (2021) 051801. [arXiv:2008.01110](#), [doi:10.1103/PhysRevLett.126.051801](#).
- [8] M. A. Acero, et al., Improved measurement of neutrino oscillation parameters by the NOvA experiment, Phys. Rev. D 106 (3) (2022) 032004. [arXiv:2108.08219](#), [doi:10.1103/PhysRevD.106.032004](#).
- [9] K. Abe, et al., Improved constraints on neutrino mixing from the T2K experiment with 3.13×10^{21} protons on target, Phys. Rev. D 103 (11) (2021) 112008. [arXiv:2101.03779](#), [doi:10.1103/PhysRevD.103.112008](#).
- [10] P. B. Denton, A. Giarnetti, D. Meloni, How to identify different new neutrino oscillation physics scenarios at DUNE, JHEP 02 (2023) 210. [arXiv:2210.00109](#), [doi:10.1007/JHEP02\(2023\)210](#).
- [11] M. A. Acero, et al., Search for CP-Violating Neutrino Nonstandard Interactions with the NOvA Experiment, Phys. Rev. Lett. 133 (20) (2024) 201802. [arXiv:2403.07266](#), [doi:10.1103/PhysRevLett.133.201802](#).
- [12] J. Kleykamp, L. R. Prais, M. A. Acero Ortega, G. S. Davies, Non-standard interactions at NOvA (2022). [doi:10.2172/1874281](#).

- [13] J. A. B. Coelho, W. A. Mann, S. S. Bashar, Nonmaximal θ_{23} mixing at NOvA from neutrino decoherence, Phys. Rev. Lett. 118 (22) (2017) 221801. [arXiv:1702.04738](#), [doi:10.1103/PhysRevLett.118.221801](#).
- [14] V. De Romeri, C. Giunti, T. Stuttard, C. A. Ternes, Neutrino oscillation bounds on quantum decoherence, JHEP 09 (2023) 097. [arXiv:2306.14699](#), [doi:10.1007/JHEP09\(2023\)097](#).
- [15] I. Singh, P. Singh, B. Choudhary, Impact of High Energy νe ($\nu^- e$) Events on NOvA Oscillation Sensitivities, Springer Proceedings in Physics 304 (2024) 174–178. [doi:10.1007/978-981-97-0289-3_37](#).
- [16] P. N. Shanahan, P. L. Vahle, Physics with NOvA: a half-time review, Eur. Phys. J. ST 230 (24) (2021) 4259–4273. [doi:10.1140/epjs/s11734-021-00285-9](#).
- [17] P. Huber, M. Lindner, W. Winter, Simulation of long-baseline neutrino oscillation experiments with GLoBES (General Long Baseline Experiment Simulator), Comput. Phys. Commun. 167 (2005) 195. [arXiv:hep-ph/0407333](#), [doi:10.1016/j.cpc.2005.01.003](#).
- [18] P. Huber, J. Kopp, M. Lindner, M. Rolinec, W. Winter, New features in the simulation of neutrino oscillation experiments with GLoBES 3.0: General Long Baseline Experiment Simulator, Comput. Phys. Commun. 177 (2007) 432–438. [arXiv:hep-ph/0701187](#), [doi:10.1016/j.cpc.2007.05.004](#).
- [19] M. A. Acero, et al., New constraints on oscillation parameters from ν_e appearance and ν_μ disappearance in the NOvA experiment, Phys. Rev. D 98 (2018) 032012. [arXiv:1806.00096](#), [doi:10.1103/PhysRevD.98.032012](#).
- [20] M. A. Acero, et al., First Measurement of Neutrino Oscillation Parameters using Neutrinos and Antineutrinos by NOvA, Phys. Rev. Lett. 123 (15) (2019) 151803. [arXiv:1906.04907](#), [doi:10.1103/PhysRevLett.123.151803](#).
- [21] J. Kopp, Efficient numerical diagonalization of hermitian 3 x 3 matrices, Int. J. Mod. Phys. C 19 (2008) 523–548. [arXiv:physics/0610206](#), [doi:10.1142/S0129183108012303](#).
- [22] J. Kopp, M. Lindner, T. Ota, J. Sato, Non-standard neutrino interactions in reactor and super-beam experiments, Phys. Rev. D 77 (2008) 013007. [arXiv:0708.0152](#), [doi:10.1103/PhysRevD.77.013007](#).
- [23] G. L. Fogli, E. Lisi, A. Marrone, D. Montanino, A. Palazzo, Getting the most from the statistical analysis of solar neutrino oscillations, Phys. Rev. D 66 (2002) 053010. [arXiv:hep-ph/0206162](#), [doi:10.1103/PhysRevD.66.053010](#).

- [24] P. Huber, M. Lindner, W. Winter, Superbeams versus neutrino factories, Nucl. Phys. B 645 (2002) 3–48. [arXiv:hep-ph/0204352](#), [doi:10.1016/S0550-3213\(02\)00825-8](#).
- [25] M. Tanabashi, et al., Review of Particle Physics, Phys. Rev. D 98 (3) (2018) 030001. [doi:10.1103/PhysRevD.98.030001](#).
- [26] Y. Farzan, M. Tortola, Neutrino oscillations and Non-Standard Interactions, Front. in Phys. 6 (2018) 10. [arXiv:1710.09360](#), [doi:10.3389/fphy.2018.00010](#).
- [27] C. Biggio, M. Blennow, E. Fernandez-Martinez, General bounds on non-standard neutrino interactions, JHEP 08 (2009) 090. [arXiv:0907.0097](#), [doi:10.1088/1126-6708/2009/08/090](#).
- [28] T. Ohlsson, Status of non-standard neutrino interactions, Rept. Prog. Phys. 76 (2013) 044201. [arXiv:1209.2710](#), [doi:10.1088/0034-4885/76/4/044201](#).
- [29] O. G. Miranda, H. Nunokawa, Non standard neutrino interactions: current status and future prospects, New J. Phys. 17 (9) (2015) 095002. [arXiv:1505.06254](#), [doi:10.1088/1367-2630/17/9/095002](#).
- [30] Neutrino Non-Standard Interactions: A Status Report, Vol. 2. [arXiv:1907.00991](#), [doi:10.21468/SciPostPhysProc.2.001](#).
- [31] C. Bera, K. N. Deepthi, R. Mohanta, The effect of non-standard interactions and environmental decoherence at DUNE (1 2025). [arXiv:2501.14383](#).
- [32] T. Stuttard, M. Jensen, Neutrino decoherence from quantum gravitational stochastic perturbations, Phys. Rev. D 102 (11) (2020) 115003. [arXiv:2007.00068](#), [doi:10.1103/PhysRevD.102.115003](#).
- [33] C. Giunti, C. W. Kim, Coherence of neutrino oscillations in the wave packet approach, Phys. Rev. D 58 (1998) 017301. [arXiv:hep-ph/9711363](#), [doi:10.1103/PhysRevD.58.017301](#).
- [34] M. Blennow, T. Ohlsson, W. Winter, Damping signatures in future neutrino oscillation experiments, JHEP 06 (2005) 049. [arXiv:hep-ph/0502147](#), [doi:10.1088/1126-6708/2005/06/049](#).
- [35] E. Akhmedov, D. Hernandez, A. Smirnov, Neutrino production coherence and oscillation experiments, JHEP 04 (2012) 052. [arXiv:1201.4128](#), [doi:10.1007/JHEP04\(2012\)052](#).
- [36] Y.-L. Chan, M. C. Chu, K. M. Tsui, C. F. Wong, J. Xu, Wave-packet treatment of reactor neutrino oscillation experiments and its implications on determining the neutrino mass hierarchy, Eur. Phys. J. C 76 (6) (2016) 310. [arXiv:1507.06421](#), [doi:10.1140/epjc/s10052-016-4143-4](#).

- [37] A. de Gouvêa, V. De Romeri, C. A. Ternes, Combined analysis of neutrino decoherence at reactor experiments, JHEP 06 (2021) 042. [arXiv:2104.05806](#), [doi:10.1007/JHEP06\(2021\)042](#).
- [38] G. Lindblad, On the Generators of Quantum Dynamical Semigroups, Commun. Math. Phys. 48 (1976) 119. [doi:10.1007/BF01608499](#).
- [39] V. Gorini, A. Kossakowski, E. C. G. Sudarshan, Completely Positive Dynamical Semigroups of N Level Systems, J. Math. Phys. 17 (1976) 821. [doi:10.1063/1.522979](#).
- [40] V. Gorini, A. Frigerio, M. Verri, A. Kossakowski, E. C. G. Sudarshan, Properties of Quantum Markovian Master Equations, Rept. Math. Phys. 13 (1978) 149. [doi:10.1016/0034-4877\(78\)90050-2](#).
- [41] T. Banks, L. Susskind, M. E. Peskin, Difficulties for the Evolution of Pure States Into Mixed States, Nucl. Phys. B 244 (1984) 125–134. [doi:10.1016/0550-3213\(84\)90184-6](#).
- [42] F. Benatti, H. Narnhofer, ENTROPY BEHAVIOR UNDER COMPLETELY POSITIVE MAPS, Lett. Math. Phys. 15 (1988) 325. [doi:10.1007/BF00419590](#).
- [43] P. B. Denton, S. J. Parke, Addendum to “Compact perturbative expressions for neutrino oscillations in matter”[Addendum: JHEP 06, 109 (2018)] (1 2018). [arXiv:1801.06514](#), [doi:10.1007/JHEP06\(2018\)109](#).
- [44] G. Balieiro Gomes, D. V. Forero, M. M. Guzzo, P. C. De Holanda, R. L. N. Oliveira, Quantum Decoherence Effects in Neutrino Oscillations at DUNE, Phys. Rev. D 100 (5) (2019) 055023. [arXiv:1805.09818](#), [doi:10.1103/PhysRevD.100.055023](#).
- [45] P. Coloma, J. Lopez-Pavon, I. Martinez-Soler, H. Nunokawa, Decoherence in Neutrino Propagation Through Matter, and Bounds from IceCube/DeepCore, Eur. Phys. J. C 78 (8) (2018) 614. [arXiv:1803.04438](#), [doi:10.1140/epjc/s10052-018-6092-6](#).
- [46] V. De Romeri, C. Giunti, T. Stuttard, C. A. Ternes, Neutrino oscillation bounds on quantum decoherence, JHEP 09 (2023) 097. [arXiv:2306.14699](#), [doi:10.1007/JHEP09\(2023\)097](#).
- [47] C. Bera, K. N. Deepthi, Study of quantum decoherence at the Protvino to ORCA experiment, Phys. Rev. D 110 (3) (2024) 035035. [arXiv:2405.03286](#), [doi:10.1103/PhysRevD.110.035035](#).
- [48] J. R. Ellis, N. E. Mavromatos, D. V. Nanopoulos, Quantum gravitational diffusion and stochastic fluctuations in the velocity of light, Gen. Rel. Grav. 32 (2000) 127–144. [arXiv:gr-qc/9904068](#), [doi:10.1023/A:1001852601248](#).

- [49] J. R. Ellis, N. E. Mavromatos, D. V. Nanopoulos, Quantum decoherence in a D foam background, *Mod. Phys. Lett. A* 12 (1997) 1759–1773. [arXiv:hep-th/9704169](#), [doi:10.1142/S0217732397001795](#).